INTERNATIONAL JOURNAL FOR NUMERICAL METHODS IN FLUIDS
Int. J. Numer. Meth. Fluids 2006; **51**:791–818
Published online 20 December 2005 in Wiley InterScience (www.interscience.wiley.com). DOI: 10.1002/fld.1159

Numerical analysis of turbulent structure in compound meandering open channel by algebraic Reynolds stress model

Hitoshi Sugiyama*,†, Daisuke Hitomi‡ and Takuya Saito§

Energy and Environmental Science, Graduate School of Engineering, Utsunomiya University, 7-1-2 Yoto, Utsunomiya 321-8585, Japan

SUMMARY

The turbulent flow in a compound meandering channel with a rectangular cross section is one of the most complicated turbulent flows, because the flow behaviour is influenced by several kinds of forces, including centrifugal forces, pressure-driven forces and shear stresses generated by momentum transfer between the main channel and the flood plain. Numerical analysis has been performed for the fully developed turbulent flow in a compound meandering open-channel flow using an algebraic Reynolds stress model. The boundary-fitted coordinate system is introduced as a method for coordinate transformation in order to set the boundary conditions along the complicated shape of the meandering open channel. The turbulence model consists of transport equations for turbulent energy and dissipation, in conjunction with an algebraic stress model based on the Reynolds stress transport equations. With reference to the pressure–strain term, we have made use of a modified pressure–strain term. The boundary condition of the fluctuating vertical velocity is set to zero not only for the free surface, but also for computational grid points next to the free surface, because experimental results have shown that the fluctuating vertical velocity approaches zero near the free surface. In order to examine the validity of the present numerical method and the turbulent model, the calculated results are compared with experimental data measured by laser Doppler anemometer. In addition, the compound meandering open channel is clarified somewhat based on the calculated results. As a result of the analysis, the present algebraic Reynolds stress model is shown to be able to reasonably predict the turbulent flow in a compound meandering open channel.

KEY WORDS: numerical analysis; turbulent flow; algebraic Reynolds stress model; meandering open channel; boundary-fitted coordinate system

1. INTRODUCTION

Almost all natural rivers exhibit a compound, two-stage geometry, consisting of a deep main channel flanked by one or two flood plains. When the flows in such sections exceed the main channel depth, the adjoining flood plains become inundated and carry part of the river flow.

*Correspondence to: Hitoshi Sugiyama, Energy and Environmental Science, Graduate School of Engineering, Utsunomiya University, 7-1-2 Yoto, Utsunomiya 321-8585, Japan.
†E-mail: sugiyama@cc.utsunomiya-u.ac.jp
‡E-mail: dhitomi@cc.utsunomiya-u.ac.jp
§E-mail: W020089@tohoku-epco.co.jp

Received 22 June 2005
Revised 3 November 2005
Accepted 7 November 2005

Due to different hydraulic conditions prevailing in the river and the flood plain, the mean velocity in the main channel and that in the flood plain are different. Just above the bank-full stage, the flow in the main channel experts a pulling or accelerating force on the flow over the flood plains, which naturally generates a dragging or retarding force on the flow through the main channel. This leads to the transfer of momentum between the main channel and the flood plain. This momentum transfer is closely related to the generation of the secondary flow, which is dynamically produced as a result of the imbalance between the centrifugal force and the pressure-driven force. In the case of a turbulent flow, fluctuating velocity makes the flow behaviour more complicated by means of turbulent diffusivity. Therefore, the turbulent flow in a compound meandering channel is considered to be a complicated turbulent flow. At the same time, it is important to clarify the flow behaviour of the meandering channel in order to improve design methods for flood protection and to reduce the damage to river environments caused by floods.

Research in compound open channels is classified into roughly two types based on the configuration of the channel examined. The first type is the straight channel, and the second type is the single curved channel. In these studies, special attention has been given to straight open-channel flow [1, 2], because the secondary flow of the second kind, which is produced by anisotropic turbulence, has been observed as a characteristic feature near the corners of compound cross sections. This secondary flow is generated in the turbulent flow of straight channels with non-circular cross sections. The other hand, the secondary flow of the first kind, which is driven by the pressure gradient, has been identified in curved channels. Therefore, the secondary flow of the second kind moving obliquely toward the free surface has been measured in detail near the intersection point between the flood plain bed and the bank of the main channel [3]. The turbulent flow in the single curved channel with a compound cross section has also been investigated in detail using a hot-wire anemometer [4]. In the case of the compound curved channel, another interesting phenomenon has been observed near the region where the river flows from a straight channel into a curved channel, and *vice versa*, because the secondary flow driven by the anisotropic turbulence in the straight channel transforms gradually into the secondary flow driven by the pressure gradient in the curved channel.

In contrast to the above-mentioned research into the compound open channel, few studies have examined compound meandering open channels, which are composed of several straight and curved channels. Sellin *et al.* [5] systematically measured the flow behaviour of a compound meandering channel by changing the discharge, the roughness of the flow bed and the bend angle of the meandering open channel. They established mechanisms that are important in meandering two-stage channels by examining velocity and direction data and by flow visualization tests, and the flow mechanism of the meandering two-stage channel was demonstrated schematically. Ervine *et al.* [6] presented a practical method for predicting depth-averaged velocity and shear stress for straight and meandering overbank flows. They also showed that the present method gives much better predictions of velocity and shear stress, particularly in cases in which the secondary flows are dominant. Patra and Kar [7] presented a simple and accurate method for estimating the discharge and velocity distribution in two-stage meandering compound channels from experimental data, which has been measured for a series of nine channel cross sections with changing width ratios between the compound sections and the main channel.

The above-mentioned studies are concerned with methods for estimating the discharge from the compound meandering channel, and the measurement of turbulent flow that includes

Reynolds stresses in the compound meandering channel using a laser Doppler anemometer has only recently been reported. Shiono and Muto [8] and Muto *et al.* [9] measured turbulent flow in detail for compound meandering channels with rectangular and trapezoidal cross sections and have suggested that the most interesting feature of the compound meandering channel flow is the complicated behaviour of the secondary flow. In addition to such observations, the measurement data of these studies are particularly useful not only for understanding the flow mechanisms in meandering open channels, but also for developing proper turbulence models for such complicated turbulent flows. Kiely [10] also measured turbulent flow in the compound meandering open channel using a laser Doppler anemometer. However, the measurement data were limited to the mean flow field, and data for turbulent flow including Reynolds stresses have not yet been presented. Kiely reported that the strength of the secondary flow reaches 30% of the averaged velocity over the cross section. As indicated by these experimental results, the flow behaviour in the compound meandering open channel has gradually become clearer. However, due to the complicated turbulent flow and channel configuration, predictions that include the distributions of the Reynolds stresses have not yet been presented.

Based on the above considerations, the main goal of the present research is the calculation of turbulent flow in the compound meandering channel with a rectangular cross section. The calculated results including Reynolds stresses are compared quantitatively with the experimental data reported by Shiono and Muto [8]. In the present study, an algebraic Reynolds stress model is adopted in order to predict anisotropic turbulent flow precisely, and the boundary-fitted coordinate system is introduced as a coordinate transformation method.

2. ANALYSIS

2.1. Numerical model and definition of coordinate system

Figure 1 shows schematic diagrams of the meandering open channel corresponding to one wavelength of five meandering channels that are continuously constructed in the experimental flume by Shiono and Muto [8]. In the experimental flume, five meander waves are fabricated for the case of $s = 1.37$, where the sinuosity, s, is defined as the ratio of the meandering channel length to the meander wavelength. One meander channel has following dimensions: bed width; 150 mm, main channel depth; 53 mm, bend radius; 425 mm, meander wavelength; 1848 mm, and central angle of the bend; 120°, as shown in the lower diagram of Figure 1. The experimental flume has a rectangular cross section of 1200 mm in width, 105 mm in depth and 1848 mm in length, as shown in the upper diagram of Figure 1. Shiono and Muto [8] measured the turbulent flow in the meandering channel in detail using a laser Doppler anemometer and presented the distributions of mean velocity and Reynolds stresses at seven cross sections in the meandering channel. With respect to the location of the measurement section, Shiono and Muto [8] reported that the experimental data are not influenced by the outlet cross section of the flume. The outlet cross section is located approximately 2 m downstream from the location of the measurement cross section. The Reynolds number is 4.92×10^4, based on the hydraulic radius and the bulk velocity. In the case of the present experiment, three kinds of measurement data are presented for various depths of water, from an inbank flow to an overbank flow. In this calculation, a meandering channel with a relative depth $D_r = 0.5$, which corresponds to a deep overbank flow, is used as the numerical model.

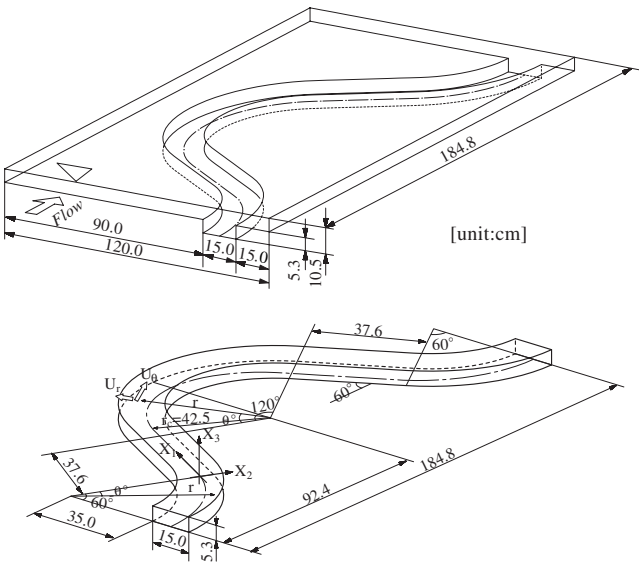

Figure 1. Compound meandering open channel and definition of coordinate system.

The coordinates system used in the calculation is also defined in Figure 1. For convenience, rectangular and cylindrical coordinates are adopted in the straight and curved open channels, respectively. In the straight open channel, the main flow direction is along the X_1-axis and the secondary flow directions are along the X_2- and X_3-axes, which represent the horizontal and vertical directions, respectively. The origin of the rectangular coordinates is set at the central point of the riverbed for the inlet cross section of the main straight channel. In addition, the upstream and downstream curved channels are distinguished by the sign of the curved bend angle, that is $\theta = -60$ and 60° denote the inlet and outlet cross sections, respectively, of the half-wavelength meandering channel.

2.2. Governing transport equations

The transport equation of momentum is expressed in the following form through ensemble averaging:

$$\frac{D\overline{U_i}}{Dt} = -\frac{1}{\rho}\frac{\partial \bar{P}}{\partial X_i} + \frac{\partial}{\partial X_j}\left(\nu \frac{\partial \overline{U_i}}{\partial X_j} - \overline{u_i u_j}\right) \tag{1}$$

The Reynolds stresses that appear in the transport equation must be solved in order to obtain the velocity fields completely.

In this calculation, we have adopted the transport equation of Reynolds stresses in order to accurately predict anisotropic turbulence. The transport equation of Reynolds stresses is displayed exactly in the following form:

$$\frac{D\overline{u_i u_j}}{Dt} = -\left(\overline{u_i u_k}\frac{\partial U_j}{\partial X_k} + \overline{u_j u_k}\frac{\partial U_i}{\partial X_k}\right) + \overline{\frac{p}{\rho}\left(\frac{\partial u_i}{\partial X_j} + \frac{\partial u_j}{\partial X_i}\right)}$$

$$-\frac{\partial}{\partial X_k}\left\{\overline{u_i u_j u_k}-\nu\frac{\partial \overline{u_i u_j}}{\partial X_k}+\overline{\frac{p}{\rho}\left(\delta_{jk}u_i+\delta_{ik}u_j\right)}\right\}-2\nu\,\overline{\frac{\partial u_i}{\partial X_k}\frac{\partial u_j}{\partial X_k}} \tag{2}$$

It is impossible to numerically solve the above equation directly, so it is necessary to rewrite several of the terms of the Reynolds stress equation by introducing the concept of the turbulent model. Moreover, with respect to the numerical analysis, the convection term of the left-hand side and the diffusion term of right-hand side of Equation (2) make it difficult to obtain a numerical solution because these terms require iterative calculations in order to obtain stable results. In the present study, these terms are modelled by adopting Rodi's [11] approximation. As a result of this approximation, these two terms are transformed into algebraic form from differencing form. Therefore, the convection and diffusion terms in the above equation were modelled as follows:

$$\frac{D\overline{u_i u_j}}{Dt}-Diff_{ij}=\frac{\overline{u_i u_j}}{2k}\left(P_k-\varepsilon\right) \tag{3}$$

where $Diff_{ij}$ corresponds to the third term on the right-hand side of Equation (1) and P_k represents the production term of the turbulent energy equation.

A particularly problematic task here is the modelling of the pressure–strain correlation equation term, which is also defined as the redistribution term and is shown as the second term on the right-hand side of Equation (1). The pressure–strain term is composed of three parts, which are the interaction of fluctuating velocities ($\pi_{ij,1}+\pi_{ji,1}$), the interaction of the mean strain with fluctuating velocities ($\pi_{ij,2}+\pi_{ji,2}$), and wall proximity effects ($\pi_{ij,\mathrm{w}}+\pi_{ji,\mathrm{w}}$). In the present calculation, we have adopted Rotta's linear return to isotropy mode for the term ($\pi_{ij,1}+\pi_{ji,1}$), as shown in Table I.

Table I. Modelling of the pressure–strain correlation term.

$\pi_{ij,1}+\pi_{ji,1}$	$-C_1\frac{\varepsilon}{k}\left(\overline{u_i u_j}-\frac{2}{3}k\delta_{ij}\right)$
$\pi_{ij,2}+\pi_{ji,2}$	$-\frac{C_2+8}{11}\left(P_{ij}-\frac{2}{3}P_k\delta_{ij}\right)+\zeta k\left(\frac{\partial U_i}{\partial x_j}+\frac{\partial U_j}{\partial x_i}\right)$
	$-\frac{8C_2-2}{11}\left(D_{ij}-\frac{2}{3}P_k\delta_{ij}\right)$
$[\pi_{ij}+\pi_{ji}]_w$	$C_1=C_1^*+C_1' f\left(\frac{L}{X_\mathrm{w}}\right)\quad C_2=C_2^*+C_2' f\left(\frac{L}{X_\mathrm{w}}\right)$
	$\zeta=\zeta^*+\zeta' f\left(\frac{L}{X_\mathrm{w}}\right)$
	$P_{ij}=-\overline{u_i u_k}\frac{\partial U_j}{\partial x_k}-\overline{u_j u_k}\frac{\partial U_i}{\partial x_k}\quad D_{ij}=-\overline{u_i u_k}\frac{\partial U_k}{\partial x_j}-\overline{u_j u_k}\frac{\partial U_k}{\partial x_i}$
	$P_k=-\overline{u_k u_l}\frac{\partial U_k}{\partial x_l}\quad f\left(\frac{L}{X_\mathrm{w}}\right)=\frac{C_\mu^{3/4}}{\kappa}\frac{k^{3/2}}{\varepsilon}\frac{1}{X_\mathrm{w}}$

For $\pi_{ij,2}$, the correlation is approximated as

$$\pi_{ij,2} = \left(\frac{\partial U_i}{\partial X_m}\right) a_{l\,j}^{m\,i} \tag{4}$$

and $a_{l\,j}^{m\,i}$ is the fourth-order tensor, which should satisfy the following kinematic constraints:

$$a_{l\,j}^{m\,i} = a_{l\,j}^{i\,m} = a_{j\,l}^{i\,m} \tag{5}$$

$$a_{l\,j}^{m\,i}\,\frac{\partial U_l}{\partial X_m} = 0 \tag{6}$$

$$a_{j\,j}^{m\,i} = 2\overline{u_m u_i} \tag{7}$$

The above constraints arise from the symmetry condition, the mass conservation law and the Green's theorem, respectively. Although the kinematic constraint of Equation (6) differs from the constraint presented by Launder *et al.* [12], we adopted Equation (6) because $\pi_{ij,2}$ is defined as the production between the fourth-order tensor and the mean strain, as given in Equation (4). Gessner and Eppich [13] also reported these constraints and described them in detail. In terms of the modelling of $(\pi_{ij,2} + \pi_{ji,2})$, the modelling process is described in detail in a previous report by Sugiyama and Hitomi [14]. Finally, the interaction of the mean strain and fluctuating velocities $(\pi_{ij,2} + \pi_{ji,2})$ is modelled as shown in Table I.

The wall effect term $(\pi_{ij,\mathrm{w}} + \pi_{ji,\mathrm{w}})$ of the turbulent stresses is modelled, as shown in Table I, by varying the model constants. In Table I, $f(L/X_\mathrm{w})$ is a function that is related to the dimensionless distance from the wall, and c and κ represent the empirical constant and the von Karman constant, respectively. The function $f(L/X_\mathrm{w})$ takes unit value near the wall and approaches zero with increasing distance from the wall. The symbol X_w is the normal distance from the wall, and L defines the length scale of turbulence. When $f(L/X_\mathrm{w})$ takes zero value, the model yields the correct Reynolds stress components for the nearly homogeneous shear flow of Champangne *et al.* [15], while $f(L/X_\mathrm{w})$ has unit value, and the magnitude of the stress components agree with the consensus of near-wall turbulence. The model constants used in this analysis are summarized in Table II.

The fourth term of the right-hand side of Equation (2) is the homogeneous part of the dissipation. The dissipation rate everywhere in the computed flow was assumed to be locally isotropic, i.e.

$$\varepsilon_{ij} = 2\nu\,\overline{\frac{\partial u_i}{\partial X_k}\,\frac{\partial u_j}{\partial X_k}} = \frac{2}{3}\,\delta_{ij}\varepsilon \tag{8}$$

Table II. Model constants of the pressure–strain correlation term.

C_1^*	C_2^*	ζ^*	C_1'	C_2'	ζ'	C_μ	κ
1.4	0.44	−0.16	−0.35	0.12	−0.1	0.09	0.42

The transport equations of turbulent energy and dissipation are expressed as follows:

$$\frac{Dk}{Dt} = \frac{\partial}{\partial X_j}\left\{\left(\nu\delta_{jk} + c_s\frac{k}{\varepsilon}\overline{u_k u_j}\right)\frac{\partial k}{\partial X_k}\right\} - \overline{u_i u_k}\frac{\partial U_i}{\partial X_k} - \varepsilon \tag{9}$$

$$\frac{D\varepsilon}{Dt} = \frac{\partial}{\partial X_j}\left\{\left(\nu\delta_{jk} + c_\varepsilon\frac{k}{\varepsilon}\overline{u_k u_j}\right)\frac{\partial \varepsilon}{\partial X_k}\right\} - \frac{\varepsilon}{k}\left(c_{1\varepsilon}\overline{u_i u_k}\frac{\partial U_i}{\partial X_k} + c_{2\varepsilon}\varepsilon\right) \tag{10}$$

Model constants c_s, c_ε, $c_{1\varepsilon}$ and $c_{2\varepsilon}$ are 0.22, 0.18, 1.44 and 1.92, respectively.

2.3. *Boundary-fitted coordinate system*

Calculation requires the boundary condition to be set precisely along the complicated shape. The boundary-fitted coordinate system is a kind of coordinate transformation method. The coordinate in the physical plane can be transformed into the coordinate in the calculation plane using the boundary-fitted coordinate system. Numerical calculation is performed in the calculation plane because it is easy to set the boundary condition along a complicated shape. In addition, the governing equations are transformed to complicated equations from simple equations expressed in the physical plane, even though it is easy to set the boundary condition along a complicated shape.

The transformation from the physical plane to the calculation plane is carried out using the following mathematics theorem:

$$\frac{\partial}{\partial X_i} = \frac{\partial \xi}{\partial X_i}\frac{\partial}{\partial \xi} + \frac{\partial \eta}{\partial X_i}\frac{\partial}{\partial \eta} + \frac{\partial \zeta}{\partial X_i}\frac{\partial}{\partial \zeta} \tag{11}$$

The symbols ξ, ζ and η represent the coordinates of the calculation plane and correspond to the main flow and the cross-sectional directions along the computational grid.

2.4. *Boundary condition for the free surface*

The method used to set the boundary condition along the free surface is also important in turbulent model in order to correctly predict anisotropic turbulence behaviour. Experimental results [16] have shown as a characteristic feature that free-surface-normal fluctuating velocity decays gradually toward the free surface. When the free-surface-normal fluctuating velocity near the free surface is compared with the wall-normal fluctuating velocity near the wall, experimental results show that the intensity of fluctuating velocity near the free surface decreases more gradually than that near the wall toward the free surface. In order to reflect this typical feature in boundary condition of the free surface, the free-surface-normal fluctuating velocity is set to zero along not only the free surface, but also the first computational grid.

The free surface is treated as a symmetric plane for dependent variables, except for the dissipation rate of the turbulent kinetic energy. As for the boundary condition of turbulent dissipation near the free surface, we introduce the wall function method, which has been used in the turbulent model for high-Reynolds numbers. The validity of the boundary condition for the free surface has been confirmed by comparing the calculated results with the experimental results of several open-channel flows [17, 18].

2.5. Numerical analysis

In the present numerical analysis of the meandering channel, the periodic boundary condition is applied in order to save computational time. Therefore, with the exception of pressure, the inlet condition is equal to the outlet condition. The derivative of pressure with respect to the main flow direction at the inlet cross section is set to be equal to that at the outlet cross section. The initial conditions of turbulent energy and dissipation were assumed to be $k = U_b^2 \times 10^{-5}$ and $\varepsilon = k^{3/2}/D$, respectively. Since the present model can be classified as a high-Reynolds-number turbulent model, the wall function method is adopted as the boundary condition for turbulent energy and dissipation at the wall.

Figure 2 shows two kinds of computational grids. The upper figure shows a top view of the grid-layout of the flume, and lower figure shows the sectional grid-layout for the main channel. The symbols ξ, ζ and η represent the coordinates of the main flow direction and the cross-sectional directions along the computational grid. The grids located near the wall are fine because the physical parameters changes rapidly near the wall. The governing equations were discretized by the differencing scheme, and QUICK (third-order upwind differencing scheme) was used for the convection term. The Reynolds number is 4.92×10^4, based on the hydraulic radius and the bulk velocity. The number of computational grid points in the total cross section is 111×31, and 70 grid points are set along the main flow direction. Therefore, the total number of computational grids is 240 870. In the curved channel, the grids are arranged

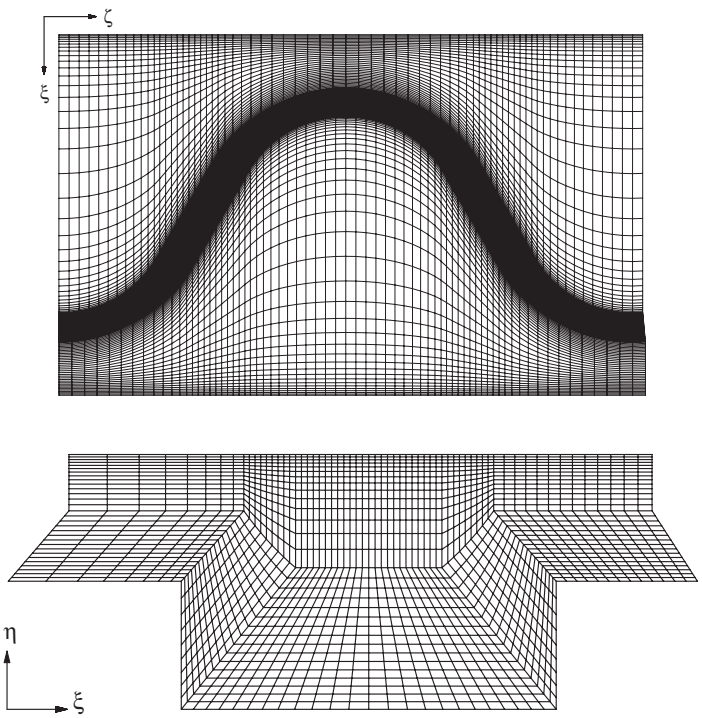

Figure 2. Computational grids layout.

in 5° intervals. The height of the free surface is assumed to be fixed in the calculation, even though it changes with the flow development because of pressure variation. The experimental data also suggest that there is almost no change in the free surface.

3. RESULTS AND DISCUSSION

3.1. Comparison of mean velocity

The calculated results for the main flow velocities are compared with the experimental data at seven stations, as shown in Figures 3(a) and (b). The results from $\theta = -60°$ until $X_1/4R = 0.94$ sections and from $\theta = 0°$ until 60° sections are shown in Figures 3(a) and (b), respectively. The $\theta = -60°$ and $-0°$ sections are equivalent in the inlet and outlet cross sections of the first curved channel located upstream in the meandering channel, respectively. Similarly, the $\theta = 0°$ and 60° sections represent the inlet and outlet cross sections of the second curved channel located down stream in the meandering channel, respectively. The symbol $X_1/4R = 0.94$ indicates the distance from the inlet cross section of the straight channel located between the first and second curved channels. Therefore, Figures 3(a) and (b) are arranged in the main flow direction from bottom to top. The calculated results and the experimental results were normalized by the bulk mean velocity. In addition, the inner and outer sides of the first curved channel correspond to left and right sides of the rectangular cross section. In the second curved channel, this relationship is reversed. The horizontal dotted line shown in the figures denotes the height of the flood plain.

The experiment considering the main flow velocity at the $\theta = -60°$ section reveals that contour lines with low values are observed mainly over the cross section of the main channel and contour lines with high value are generated in the upper layers located over the flood plain. The main meandering channel generates resistance on the entire flow field of the compound meandering open channel. The flow runs faster through regions of the channel where resistance on the entire flow cannot be generated. Therefore, the maximum velocity at the $\theta = -60°$ section is recognized not in the main channel but near the free surface over the flood plain.

With respect to the flow in the first curved channel, the experimental results show that the main flow velocity accelerates gradually as the flow develops. Acceleration of main flow velocity is especially noticeable on the inner side of the curved channel at the beginning of the first curved channel, and the maximum value is generated near the inner region of the riverbed. When the flow runs into the straight channel, the maximum velocity in the curved channel shifts to the right-hand side of the cross section of the main channel, as shown in the $X_1/4R = 0.94$ section. In addition, contour lines with fine intervals are observed along the dotted line. These distributions indicate that a shear layer with an abrupt velocity gradient is produced as a result of the interaction between the main channel flow and the flood plain flow. Comparison between the calculated and experimental results reveals that the present method is able to correctly reproduce the characteristic flow behaviours of the main flow velocity in the meandering open channel.

Comparison of the results for the second curved channel, as shown in Figure 3(b), reveals that the maximum value of the main flow velocity decreases gradually as the flow passes through the second curved channel. The experimental results for the $\theta = 30°$ section also indicate that contour lines with low values are pushed up from the centre of the riverbed

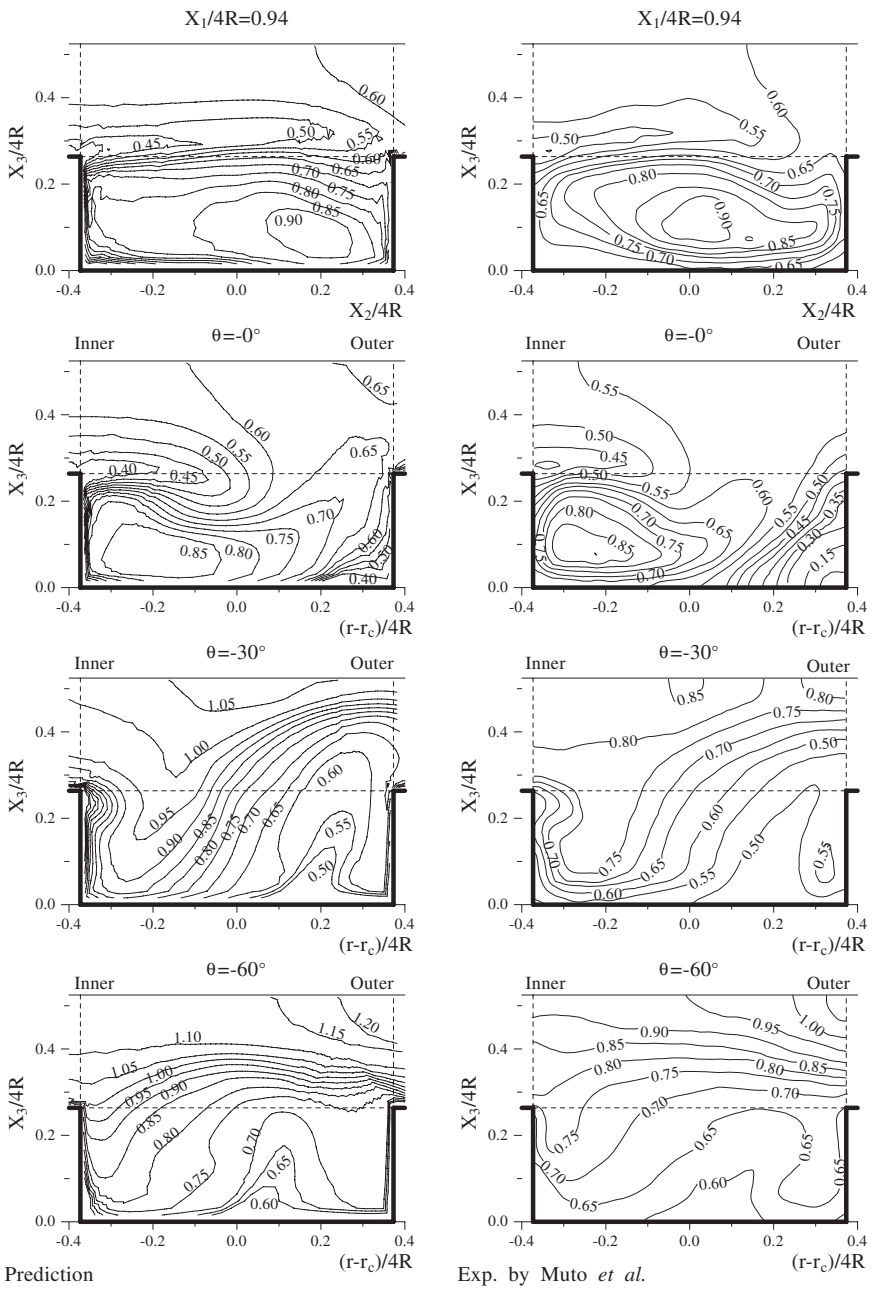

Figure 3. (a) and (b) Comparison of main flow velocity.

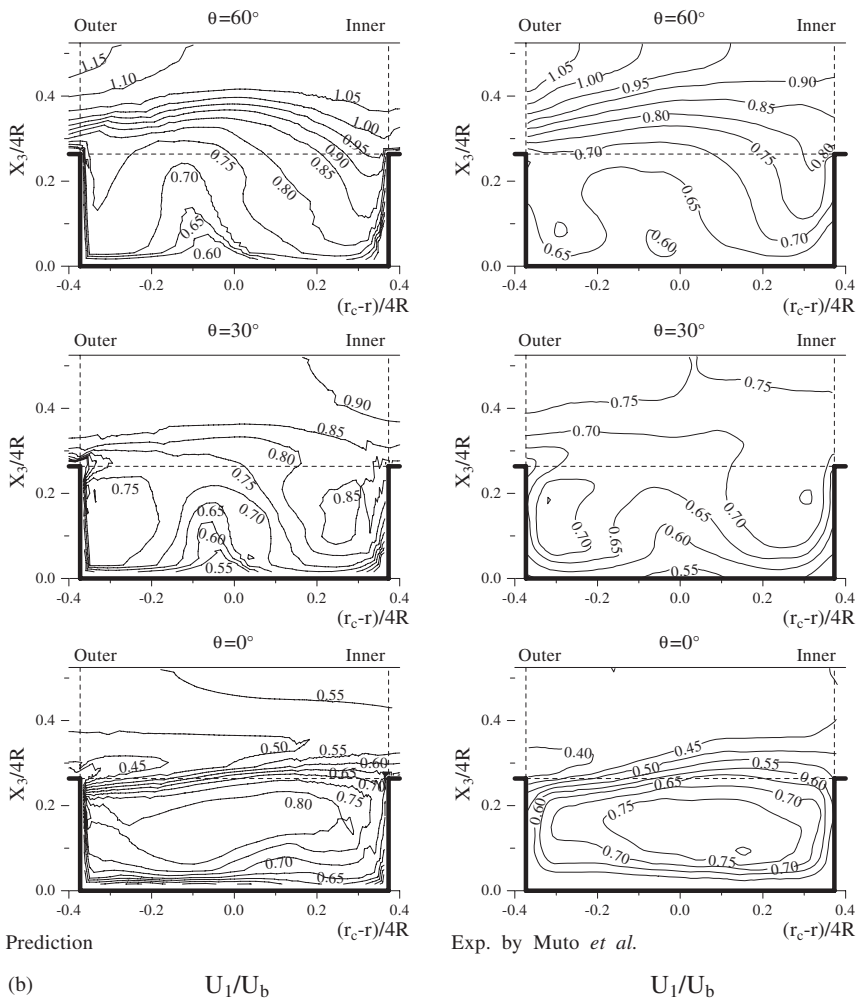

Figure 3. *Continued.*

to the free surface, forming a sort of peninsula. The present method also predicts that these characteristic features of flow behaviours exist in the second curved channel. These distorted contour lines are closely related to the flow pattern of the secondary flow.

The results of the secondary flow are arranged in two rows, as shown in Figures 4(a) and (b), in the same manner as results for the main flow velocity. The secondary flow is displayed in two-dimensional vector form. In the case of the secondary flow in a curved, closed channel, the secondary flow is caused by an imbalance between centrifugal force and pressure-gradient-driven force. However, in the case of the compound meandering channel, inflow from the flood plain to the main channel and the shear layer generated by the momentum transfer between the flood plain and the main channel play an important role in the formation of the secondary flow.

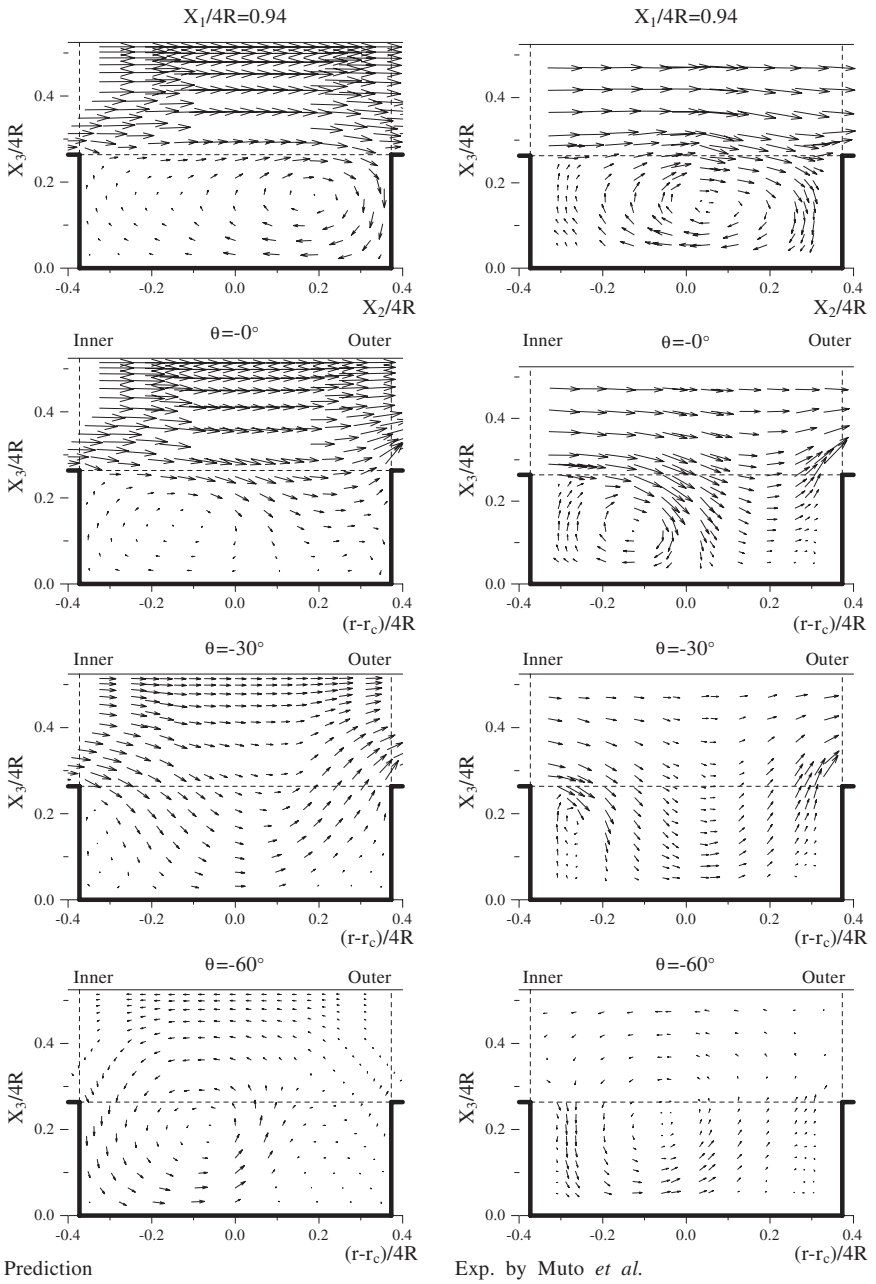

Figure 4. (a) and (b) Comparison of secondary flow.

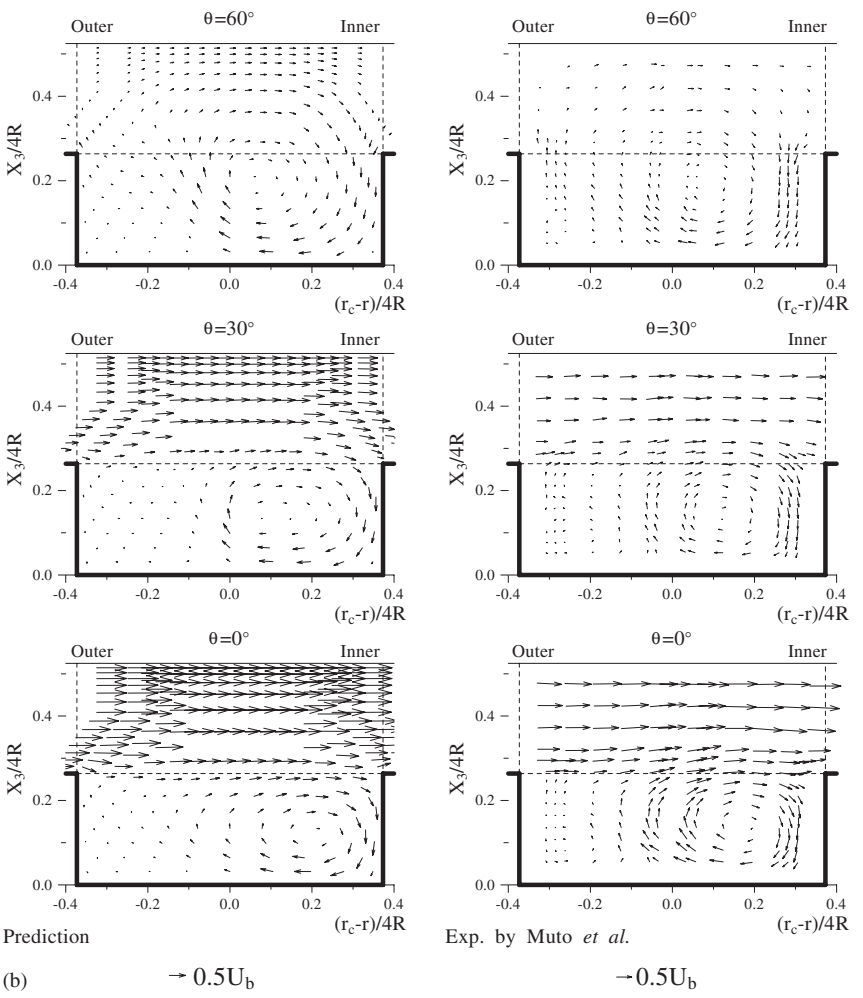

Figure 4. *Continued.*

In the first curved channel, the experimental secondary flow changes abruptly, as shown by the results between the $\theta = -60°$ and $-0°$ sections. Furthermore, the secondary flow rotates counterclockwise and is situated near the inner wall at the $\theta = -60°$ section. This circulation moves towards the outer bank as it passes downstream and disappears around the middle of the first curved channel. New clockwise circulation then starts to form at the $\theta = -0°$ section and becomes large at $X_1/4R = 0.94$ in the middle of the straight channel, i.e. the counterclockwise secondary flow observed at the $\theta = -60°$ section disappears suddenly somewhere in the first curved channel simultaneous with the appearance of a new clockwise rotating cell at the $\theta = -0°$ section. This new cell grows actively as soon as the flow runs into the straight channel and occupies most of cross section at $X_1/4R = 0.94$. At the $X_1/4R = 0.94$ section, the magnitude of the secondary flow in the upper layer is larger than that in the main

flow, and its direction is very nearly parallel to the flood plain. In addition, the flow entering from the flood plain into the main channel and the flow re-entering the flood plain from the main channel can be clearly detected near the crossing point between the side bank of the main channel and the flood plain bed, as shown in the $\theta = -30^\circ$ and -0° sections. The flow entering from the flood plain conveys high velocity flow into the main channel, whereas the re-entering flow conveys low-velocity flow from the main channel into the flood plain. This momentum transfer is closely related to the distribution of the counter lines of the main flow velocity at the $\theta = -30^\circ$ and -0° sections. Considering such momentum transfer, the secondary flow depends on both the magnitude and the angle of the flow entering the main channel. Comparison of the results suggests that the characteristic features of the secondary flow are reproduced correctly by the present method. However, a discrepancy between the results exists in that the present method tends to predict the new clockwise secondary flow to be smaller than the experimental result observed at the $\theta = -0^\circ$ section.

In the second curved channel, the magnitude of the secondary flow decreases gradually because of the reduction of inflow from the flood plain into the main channel. However, the occupied area of circulation enlarges as the flow develops downstream. Mirror images of the secondary flow distribution are attained between the consecutive bend apexes that correspond to the $\theta = -60^\circ$ and 60° sections. The calculated results are in good agreement with the experimental results. Therefore, the present numerical method coupled with an algebraic Reynolds stress model is likely to be applicable to complicated turbulent flows, such as that in the compound meandering open channel.

3.2. Comparison of Reynolds stresses distributions

Figures 5(a) and (b) show a comparison of the main flow fluctuating velocity. The calculated results and the experimental results are normalized by the averaged friction velocity over the riverbed. In the calculated results for the first curved channel, the locations of the maximum velocities at the $\theta = -60^\circ$, -30° and -0° sections are recognized near the middle, upper and outer side banks of the cross sections, respectively. These locations of the maximum velocity agree roughly with the experimental results except for the $\theta = -60^\circ$ section. As the flow passes through the straight channel, in both results, the maximum value is generated along the horizontal dotted line because of the existence of a strong shear layer that is caused by the large difference in velocity between the upper layer flow and the main channel flow. The existence of such a strong shear layer can be also predicted from the contour lines of the main flow velocity at the $X_1/4R = 0.94$ section in Figure 3(a). The steep velocity gradient of the main flow velocity produces a strong shear layer along the dotted line.

In the second curved channel, the main flow fluctuating velocity is actively generated near the horizontal dotted line in all sections, while that of the experiment is generated not only near the horizontal dotted line, but also near the inner bank side, except for the $\theta = 60^\circ$ section. Although the agreement between the calculated and experimental results is not perfect, the present method is able to reproduce the typical flow features.

Figures 6(a) and (b) show a comparison of the fluctuating horizontal velocity, which is normalized by the averaged friction velocity over the riverbed. The experimental results suggest that the region producing actively fluctuating horizontal velocity is different at each cross section. For example, the maximum velocity occurs near the riverbed of the main channel at the $\theta = -60^\circ$ section but is actively generated along the horizontal dotted line in the case of

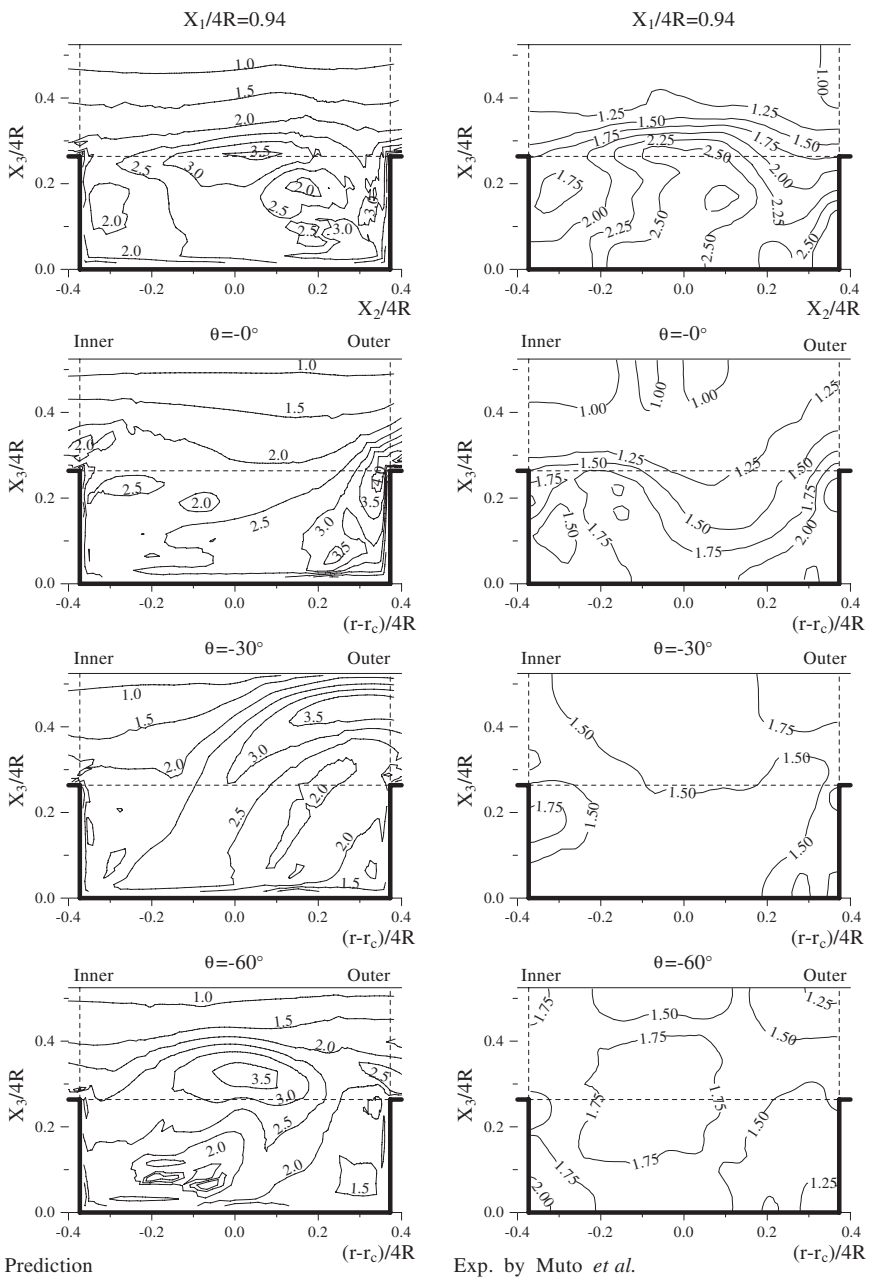

Figure 5. (a) and (b) Comparison of fluctuating velocity along the main flow direction.

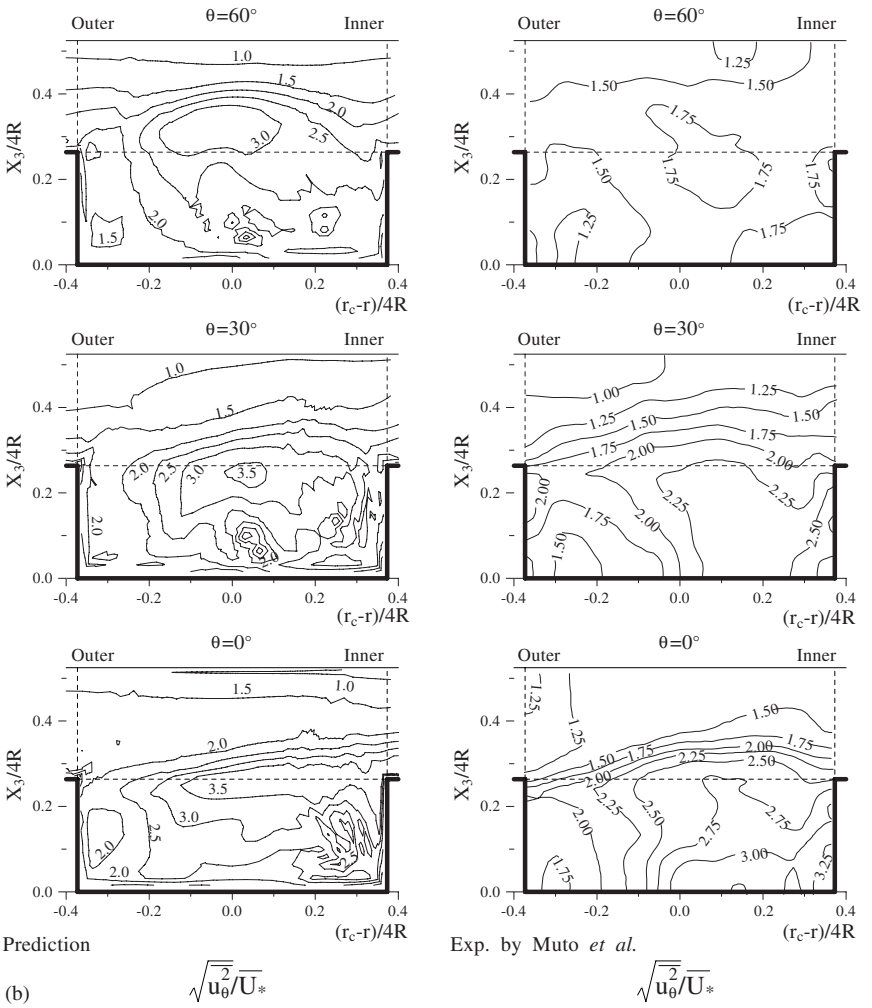

Figure 5. *Continued.*

the $X_1/4R = 0.94$ section. The maximum velocity at the $X_1/4R = 0.94$ section must be caused by the shear layer induced by the inflow from the flood plain to the main channel as well as by the main flow fluctuating velocity. Compared with the experimental result, maximum velocity locations are recognized clearly not only near the upper part of the outer bank wall but also in the central region of the main channel, as shown by the calculated result for the $\theta = -30°$ section. In addition, the calculated location of the maximum velocity at the $\theta = -0°$ section is observed only near the upper part of the outer bank wall.

In the second curved channel, the experimental results show that the greater part of the cross section at the $\theta = 0°$ and $30°$ planes is covered by contour lines with great values. However, these contour lines with great values are suddenly limited to the area near the riverbed as

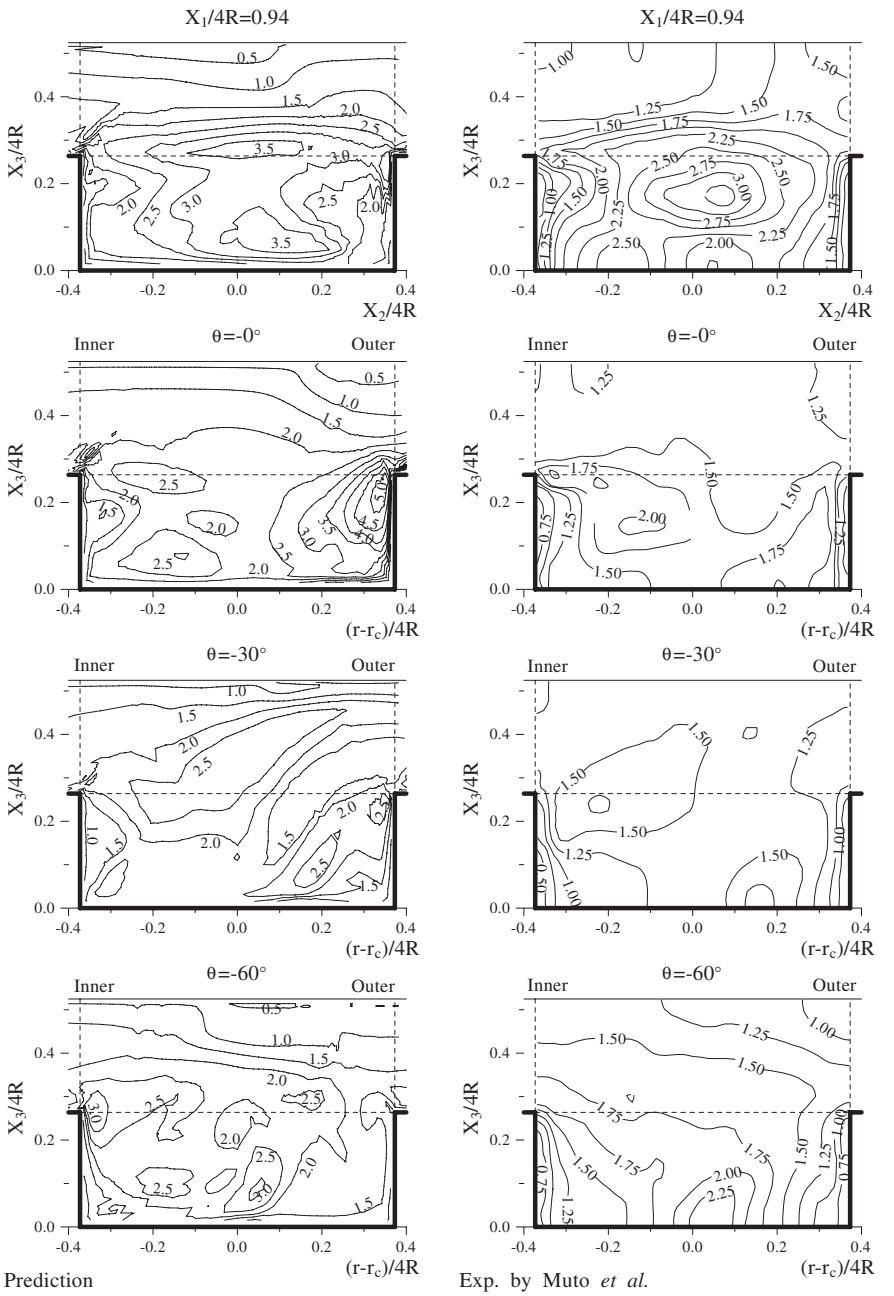

Figure 6. (a) and (b) Comparison of fluctuating velocity along the horizontal direction.

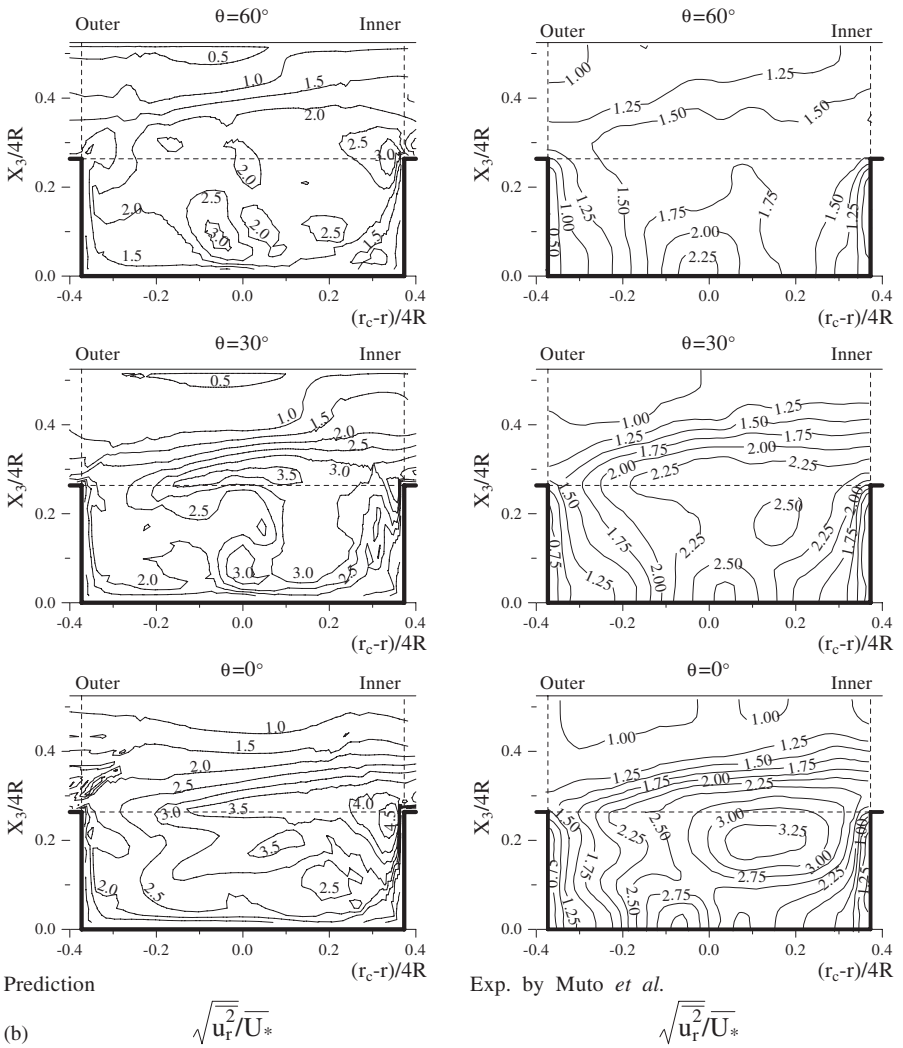

Figure 6. *Continued.*

soon as the flow reaches the $\theta = 60°$ section. The present method is also able to reproduce these features with no great discrepancies.

Figures 7(a) and (b) show the calculated and experimental distributions of the fluctuating vertical velocity, which are normalized by the averaged friction velocity over the riverbed as well as the other Reynolds stress. With respect to fluctuating velocity, it has generally been reported that the fluctuating velocity in a straight closed-duct is actively generated along the wall, which is located parallel to the direction of the fluctuating velocity, because the wall located parallel to the direction of the fluctuating velocity does not act as a barrier to the production of fluctuating velocity. However, the overall distributions in the first curved

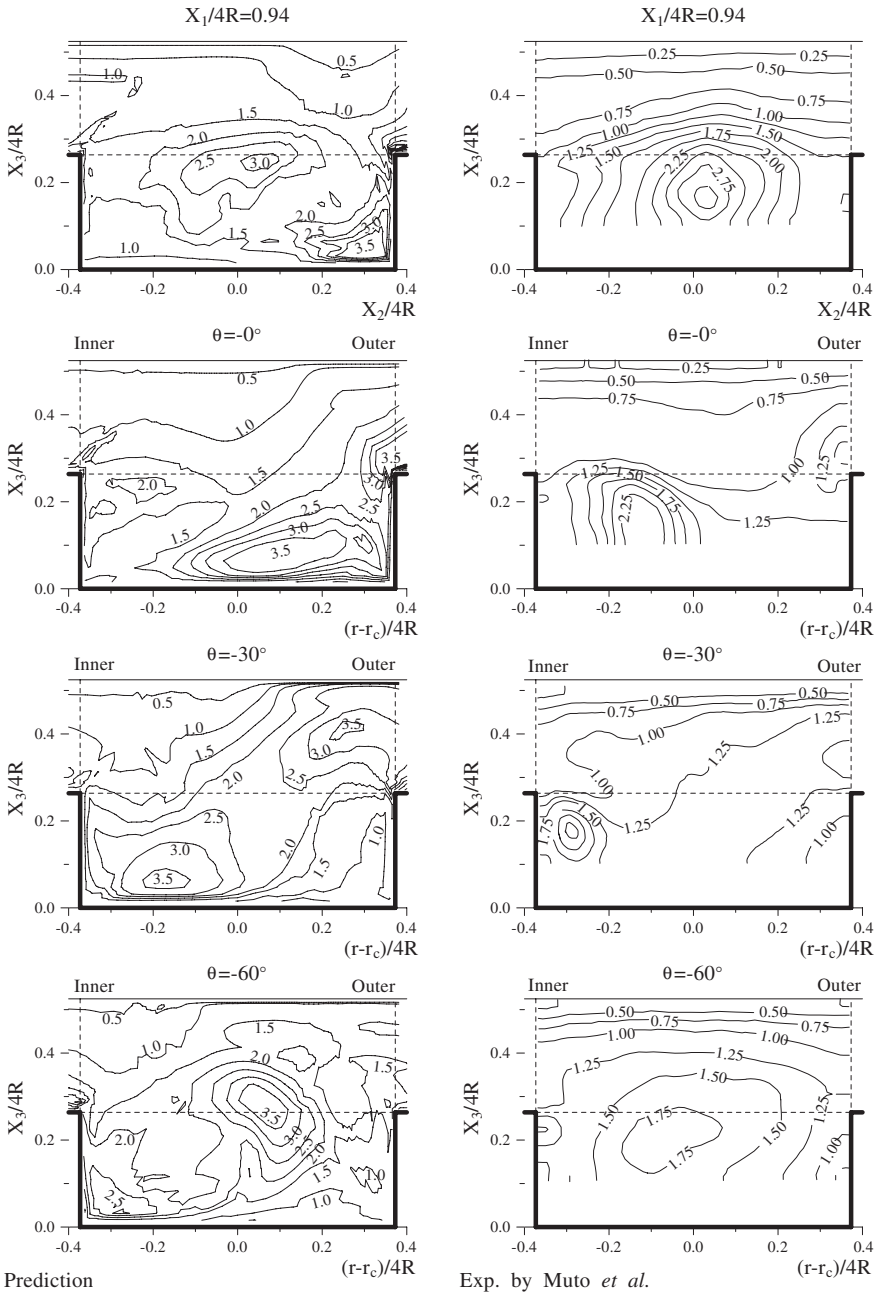

Figure 7. (a) and (b) Comparison of fluctuating velocity along the vertical direction.

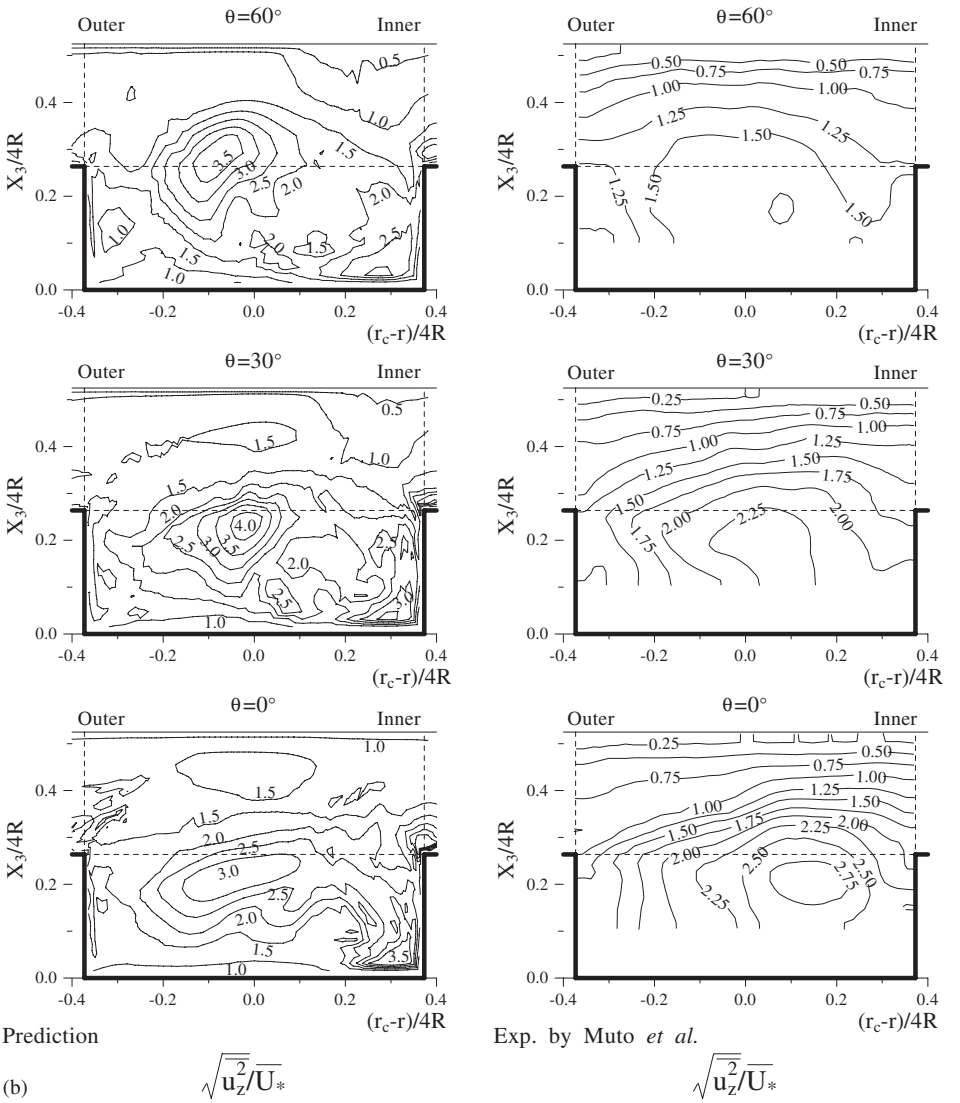

Figure 7. *Continued.*

channel indicate that contour lines with relatively large values are formed not along the vertical wall but rather in the central region of the cross sections. Therefore, these contour maps are considered as a special case of the compound meandering channel. Although it is also possible to predict these features by calculation, calculation tends to overestimate the maximum velocities, for example, the calculated maximum velocity at the $\theta = -60°$ and $-30°$ sections is approximately twice as large as that in the experiment. Such peculiar features in the first curved channel are observed in the second curved channel as well in both the calculated and experimental results.

The production term of the fluctuating vertical velocity is exactly expressed by the following equation:

$$-2\overline{u_r u_Z}\frac{\partial U_Z}{\partial r} - \frac{2\overline{u_\theta u_Z}}{r}\frac{\partial U_Z}{\partial \theta} - 2\overline{u_Z^2}\frac{\partial U_Z}{\partial Z} \tag{12}$$

Judging from the active momentum transfer between the main channel and flood plain flows, the second term involving shear stress $\overline{u_\theta u_Z}$ is predicted to play an important role in the production of fluctuating vertical velocity. As such, the location of the maximum fluctuating vertical velocity agrees roughly with that of the absolute maximum fluctuating vertical velocity for shear stress $\overline{u_\theta u_Z}$.

The calculated distributions of shear stress $\overline{u_\theta u_Z}$ between the main flow and horizontal directions are compared with the experimental distributions in Figures 8(a) and (b). As mentioned in the previous paragraph, two types of locations, the location of the maximum fluctuating vertical velocity and the location of the absolute maximum value for shear stress $\overline{u_\theta u_Z}$, coincide at each cross section. This agreement is more clearly recognizable in the case of calculation, compared to the experiment. Therefore, shear stress $\overline{u_\theta u_Z}$ contributes to the production of the fluctuating vertical velocity, and *vice versa*. The results of comparison indicate that the present method tends to overestimate experimental result in most cross sections. Considering that the production of shear stress depends greatly on the main flow velocity gradient with respect to the vertical direction, the calculation predicts the velocity gradient more steeply than the experiment, as shown in Figures 3(a) and (b). Such discrepancies may be caused by approximating the convection and diffusion terms of the Reynolds stress transport equation. These two terms are transformed to algebraic form from differencing form.

In contrast, the calculation can reproduce well the contour lines with zero value at each cross section. Contour lines with zero value are observed at each cross section, except at the $\theta = -60°$ and $60°$ sections. For example, contour lines with zero value observed at the $\theta = -30°$ and $30°$ sections are recognized near the inner bank and the outer bank, respectively, in both results. These contour lines depend on the distribution of the main flow velocity, which is distorted by the secondary flow, because the sign of shear stress $\overline{u_\theta u_Z}$ is controlled mainly by the sign of the velocity gradient $\partial U_\theta/\partial Z$, which consists of the production term of shear stress. Therefore, it is essential to predict precisely the secondary flow in order to predict well the contour lines with zero value.

Figures 9(a) and (b) show the comparison results for shear stress $\overline{u_\theta u_r}$, which is normalized by the averaged friction velocity over the riverbed. Comparing the distribution of shear stress $\overline{u_\theta u_r}$ with that of shear stress $\overline{u_\theta u_Z}$ reveals a common feature whereby the distributions contain both positive and negative regions divided by contour lines with zero value. However, contour lines with zero value are recognized in all sections of the meandering channel in the case of shear stress $\overline{u_\theta u_r}$, which differs from the distribution of shear stress $\overline{u_\theta u_Z}$. Comparing the calculated results with the experimental results, a large absolute value is measured at the $X_1/4R = 0.94$ and $\theta = 0°$ sections through all cross sections. In contrast to the experimental results, the calculation predicts a relatively large absolute value at all cross sections. The present method has a tendency to overestimate the experimental results.

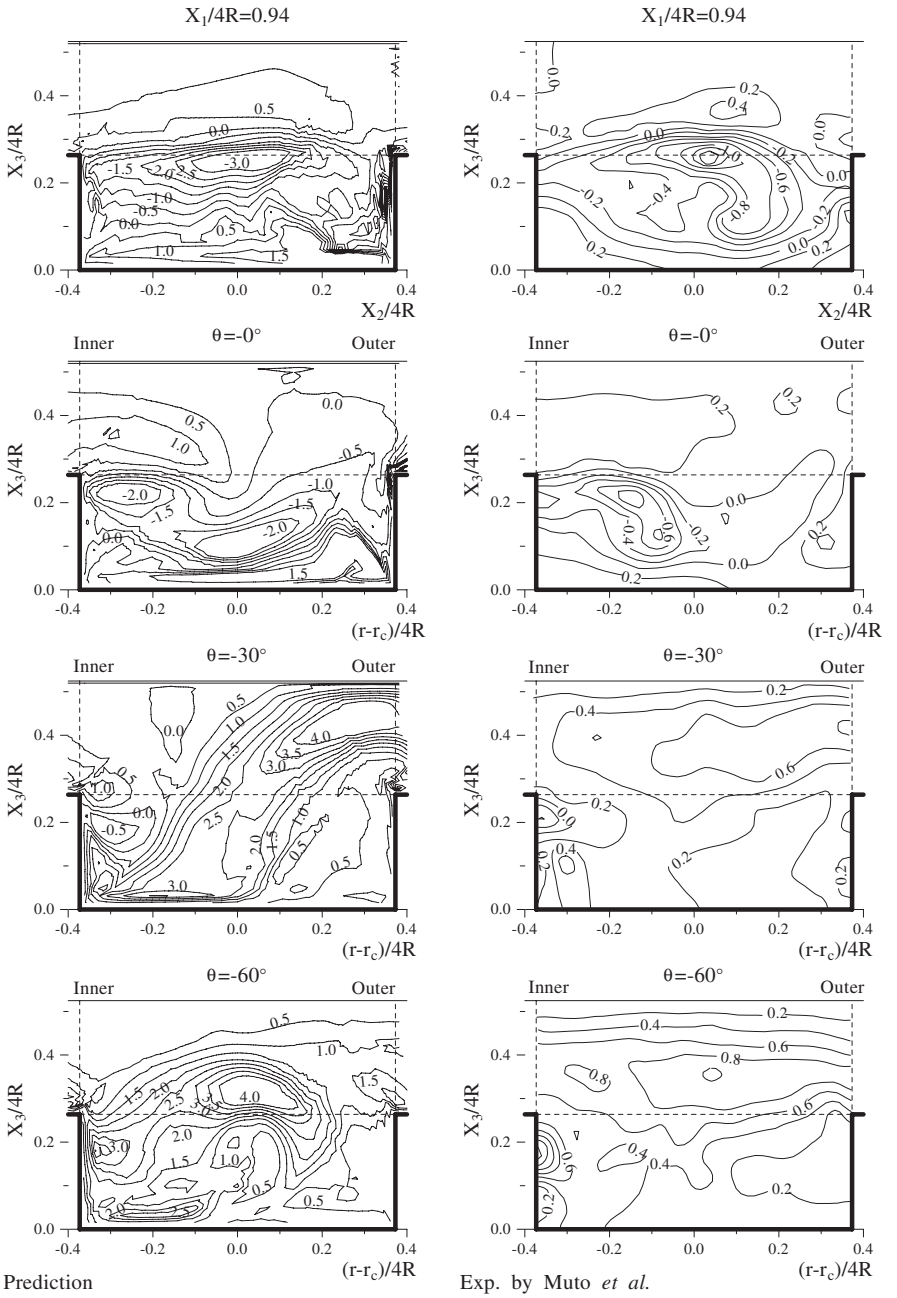

Figure 8. (a) and (b) Comparison of shear stress $\overline{u_\theta u_Z}$ between the main flow and vertical directions.

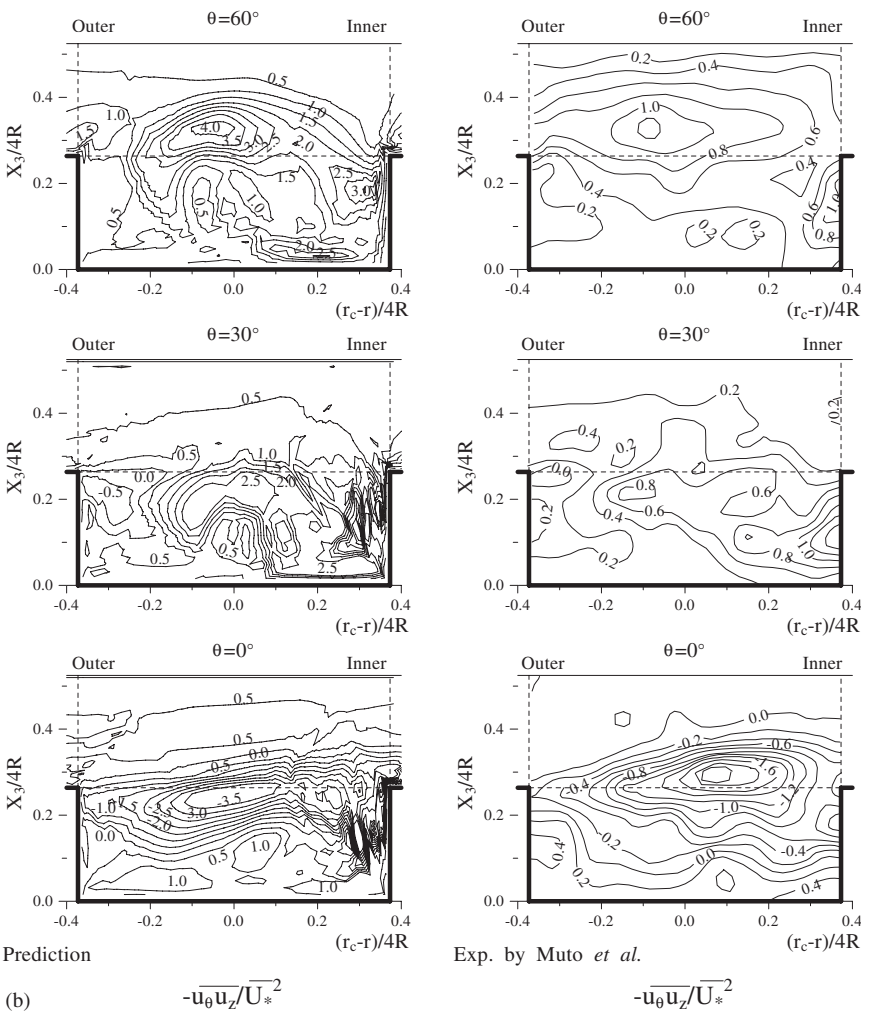

Figure 8. *Continued.*

3.3. Calculated distribution of wall shear stress

The distribution of wall shear stress over the riverbed in a meandering channel is complicated because erosive action is strongly correlated with the distribution of wall shear stress. Therefore, erosive action is promoted actively over the riverbed where the wall shear stress is large. In addition, eroded sand is conveyed by the main flow velocity and complicated secondary flow and deposited at a location downstream. Determining the distribution of wall shear stress requires knowledge of the location of erosive action. Since measuring the distribution of wall shear stress over the riverbed is difficult experimentally, the wall shear stress is estimated based on calculated results. The distributions of wall shear stress for the riverbed and bank are shown in Figure 10. The local wall shear stress is calculated by assuming a

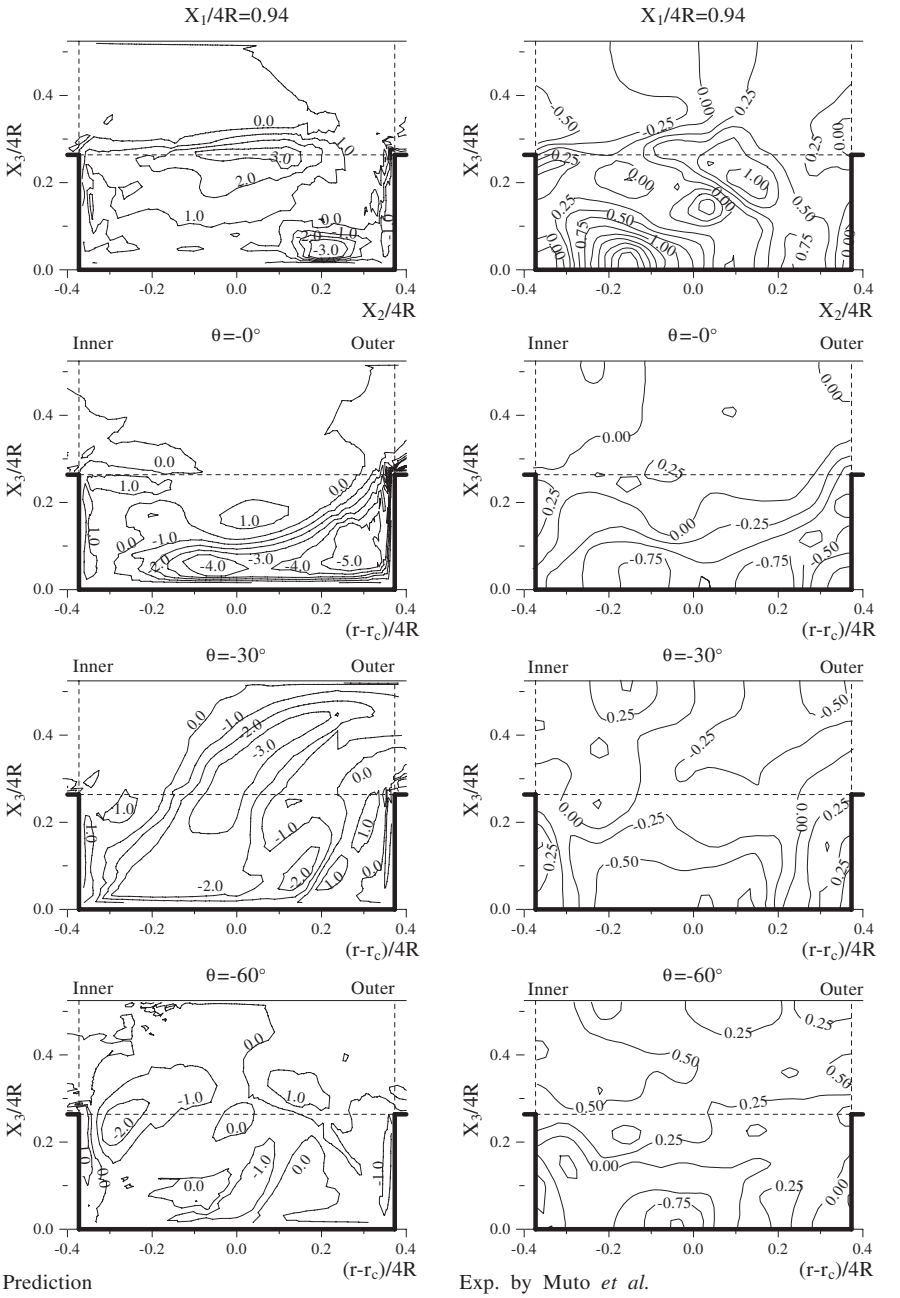

Figure 9. (a) and (b) Comparison of shear stress $\overline{u_\theta u_r}$ between the main flow and horizontal directions.

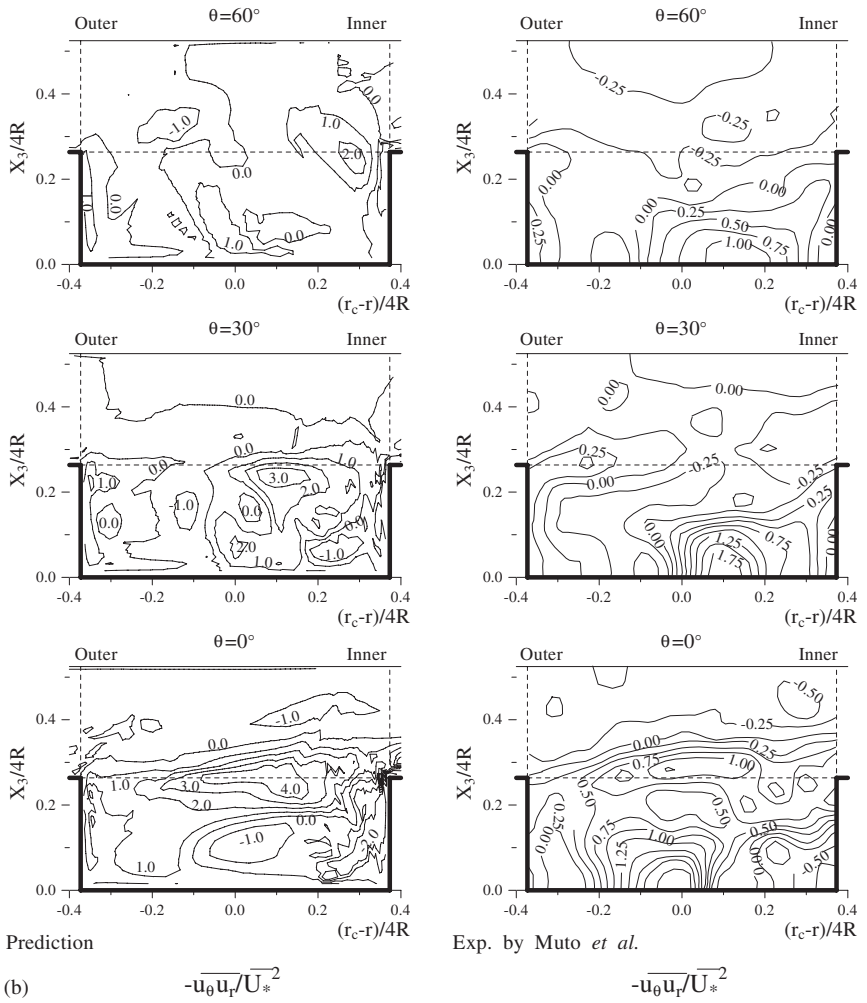

Figure 9. *Continued.*

log-law velocity profile and is normalized by the averaged velocity over the cross section. In Figure 10, the horizontal axis represents the distance from the inlet section, which is normalized by four times the hydraulic radius. The wall shear stresses for the right and left banks of the main channel are shown in the lower and upper sides of the figure, respectively. The right- and left-hand sides are defined as setting the viewpoint upstream in the meandering channel.

The maximum wall shear stress was found to be generated over the riverbed located near the right bank in the straight open channel. This region agrees with the region where the momentum transfer between the main channel and the flood plain is actively produced. Therefore, this phenomenon must be induced by the movement of the high-velocity main flow, which is caused by a strong secondary flow. As shown in Figure 3(a), the main flow

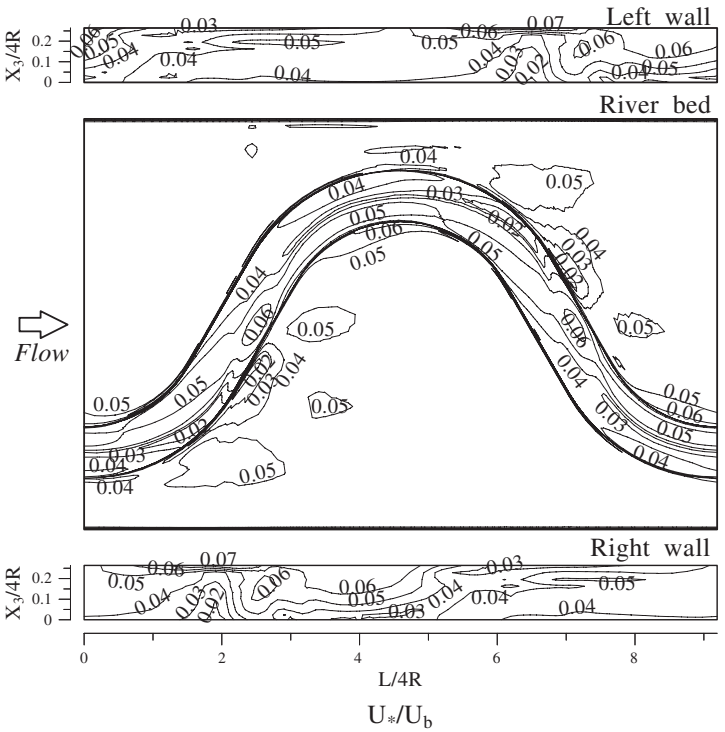

Figure 10. Calculated distribution of friction velocity.

velocity at the $X_1/4R = 0.94$ section is maximum near the right-side bank in the straight open channel.

When the distribution of wall shear stress over the right-side bank is compared to that over the left-side bank in the half-wavelength channel of the main channel located upstream, the wall shear stress of the right-side wall is larger than that of the left-side wall. This feature is especially noticeable in the straight open channel and the second curved channel. These calculated results suggest that right-side wall should be better protected from flooding than the left-side wall.

According to the distribution of wall shear stress in the flood plain, relatively large wall shear stresses are produced locally over a limited region of the flood plain slightly downstream of the meandering channel. In addition, the calculated distribution indicates that erosive action does not occur actively over the flood plain in this type of compound meandering channel with a relative depth of $D_r = 0.5$.

4. CONCLUSIONS

A numerical analysis of the three-dimensional turbulent flow in a compound meandering channel with a rectangular cross section was performed using an algebraic Reynolds stress model

and a boundary-fitted coordinate system. Calculated results were compared quantitatively with the experimental data reported by Shiono and Muto [8] in order to confirm the validity of the present method and to clarify the flow mechanism theoretically. The numerical analysis revealed the following:

(1) The present method is able to qualitatively predict the experimental features of main flow velocity in a compound meandering channel. For example, the calculation predicts well the distorted contour lines in the main channel, which are caused by the inflow from the flood plain to the main channel.
(2) Since the distribution of the secondary flow depends mainly on the magnitude and the angle of the flow entering from the flood plain into the main channel, it is essential to correctly predict the momentum transfer between the main channel and the flood plain in order to reproduce the distribution of the secondary flow. The calculated results indicate that the present method can correctly reproduce such complicated secondary flow behaviour.
(3) The experimental results for three kinds of velocity fluctuations revealed that the relative large velocity fluctuations over the meandering channel are generated in the middle of the straight channel because of the existence of a high shear layer that is produced by the inflow from the flood plain. Although such characteristic features can also be predicted by calculation, the present calculation tends to overestimate the experimental results in most cross sections.
(4) The distributions of shear stresses show both negative and positive regions in the cross section as a result of a zero contour line. The present method also predicts well these negative and positive regions. However, the calculation is unable to predict the experimental results quantitatively.
(5) The distributions of local wall shear stress over the riverbed are obtained by calculation and suggest that the inner bank requires more protection than the outer bank.
(6) Comparison with experimental data revealed that the present algebraic Reynolds stress model is applicable for the reasonable prediction of turbulent flow in a compound meandering open-channel flow.

NOMENCLATURE

B	total channel width
D_r	relative depth $(H-h)/H$
h	height of the flood plain
H	water depth of the main channel
k	turbulent energy
p	fluctuating pressure
P	mean pressure
r	radius
r_c	central radius of the bend channel
R	hydraulic radius
Re	Reynolds number $4RU_b/\nu$
t	time

$\overline{u_i u_j}$	Reynolds stresses
u_θ, u_r, u_Z	fluctuating velocity in the θ, r and Z directions
U_θ, U_r, U_Z	mean velocity in the θ, r and Z directions
U_b	bulk velocity
U_*	friction velocity
X_i	coordinate in the X_i-axis direction
Z	coordinate in the vertical direction
$\overline{(\ )}$	ensemble-averaged value

Greek letters

δ_{ij}	Kronecker delta
ε	turbulent dissipation
θ	bend angle
ν	kinematics viscosity

REFERENCES

1. Townsent DR. An investigation of turbulence characteristics in a river model of complex cross section. *Proceedings of the Institution of Civil Engineers* 1968; **40**:155–175.
2. Prinos P, Townsent DR, Tavoularis S. Structure of turbulence in compound channel flows. *Journal of Hydraulic Engineering* (ASCE) 1985; **111-9**:1246–1261.
3. Tominaga A, Nezu I. Turbulent structure in compound open-channel flows. *Journal of Hydraulic Engineering* (ASCE) 1991; **117-1**:21–41.
4. Imamoto H, Ishigaki T, Fujisawa H. On the characteristics of open channel flow in bend with flood plains. *Annuals of the Disaster Prevention Research Institute*, Kyoto University, vol. 25-B-2, 1982; 529–543 (in Japanese).
5. Sellin HJ, Ervine DA, Willetts BB. Behavior of meandering two-stage channels. *Proceedings of the Institution of Civil Engineers* 1993; **101**:99–101.
6. Ervine DA, Babaeyan-Koopaei K, Sellin HJ. Two dimensional solution for straight and meandering overbank flow. *Journal of Hydraulic Engineering* (ASCE) 2000; **126-9**:653–669.
7. Patra KC, Kar SK. Flow interaction of meandering river with floodplains. *Journal of Hydraulic Engineering* (ASCE) 2000; **126-8**:593–604.
8. Shiono K, Muto Y. Complex flow mechanisms in compound meandering channels with overbank flow. *Journal of Fluid Mechanics* 1998; **376**:221–261.
9. Muto Y, Shiono K, Imamoto H, Ishigaki T. A study on the flow in compound meandering channels (1). *Annuals of the Disaster Prevention Research Institute*, Kyoto University, vol. 38-B-2, 1995; 561–581 (in Japanese).
10. Kiely G. Overbank flow in meandering compound channels. The important mechanisms. *International Conference on River Flood Hydraulics*, Wallingford, 1990; 207–217.
11. Rodi W. A new algebraic relation for calculating the Reynolds stresses. *Zeitschrift fur Angewandte Mathematik und Mechanik* 1976; **56**:219–221.
12. Launder BE, Reece GJ, Rodi W. Progress in the development of a Reynolds stress turbulent closure. *Journal of Fluid Mechanics* 1975; **22**:537–566.
13. Gessner FB, Eppich HM. A near-wall pressure–strain model for turbulent corner flows. *Proceedings of the Third Symposium on Turbulent Shear Flows*, The University of California, Davis, 1981; 25–32.
14. Sugiyama H, Hitomi D. Numerical analysis of developing turbulent flow in a 180 bend tube by an algebraic Reynolds stress model. *International Journal for Numerical Methods in Fluids* 2005; **47**:1431–1449.
15. Champangne FH, Harris VG, Corrisn S. Experimental on nearly homogeneous turbulent shear flow. *Journal of Fluid Mechanics* 1970; **41**:81–139.
16. Nakagawa H, Nezu I, Ueda H. Turbulence of open channel flow over smooth and rough beds. *Proceedings of the Japan Society of Civil Engineers* 1975; **241**:155–168 (in Japanese).
17. Sugiyama H, Akiyama M, Matsubara T. Numerical simulation of compound open channel flow on turbulence with a Reynolds stress model. *Proceedings of the Japan Society of Civil Engineers* 1995; **515**/**II-31**:55–65 (in Japanese).
18. Sugiyama H, Akiyama M, Kamezawa M. Numerical study of turbulence structure in curved open-channel. *Proceedings of the Japan Society of Civil Engineers* 1997; **572**/**II-40**:11–21 (in Japanese).

